Exploring ion mobility mechanisms in poly indolequinone polymers: a case study on black soldier fly melanin

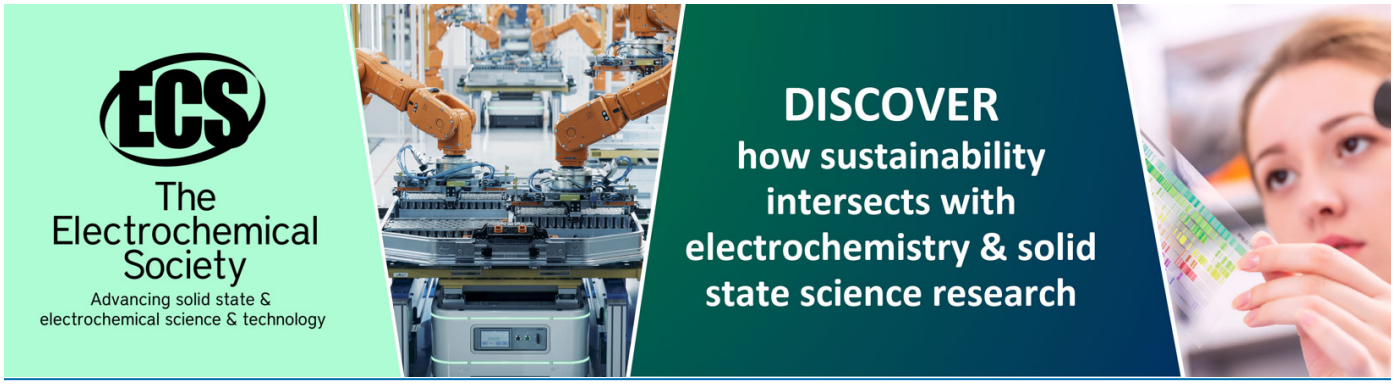

OPEN ACCESS
IOP Publishing
Journal of Physics D: Applied Physics
J. Phys. D: Appl. Phys. **57** (2024) 265303 (13pp)
https://doi.org/10.1088/1361-6463/ad3765

Exploring ion mobility mechanisms in poly indolequinone polymers: a case study on black soldier fly melanin

M Ambrico[1,*], A B Mostert[2], P F Ambrico[1], J Phua[4], S Mattiello[1,3] and R Gunnella[3]

[1] CNR-Institute for Plasma Science and Technology, Bari Branch, Via Amendola 122/D, I-70125 Bari, Italy
[2] Centre for Integrative Semiconductor Materials, Department of Physics, Swansea University Bay Campus, Fabian Way, Swansea SA1 8EN, United Kingdom
[3] School of Science and Technology University of Camerino, Via Madonna delle Carceri, 9I-62032 Camerino, MC, Italy
[4] Insectta Pte. Ltd, 8 Cleantech Loop, Singapore 637145, Singapore

E-mail: marianna.ambrico@cnr.it

Received 4 December 2023, revised 29 February 2024
Accepted for publication 25 March 2024
Published 5 April 2024

Abstract

Black soldier fly (BSF) melanin is a new supply of the brown-black pigment eumelanin. Given that eumelanin is a model bioelectronic material for applications such as medical devices and sensors, understanding BSF melanin's electrical properties is important to confirm its viability as an advanced material. Presented here is a systematic, hydration dependent alternating current study of BSF melanin utilising both H_2O and D_2O vapours. There is a clear difference between the vapours, enabling a thorough analysis including Nyquist plots with model circuit analysis, broad band dielectric spectroscopic modelling as well as applying the Trukhan model to understand free ion concentration and mobility changes as a function of hydration. We find that BSF melanin behaves similarly to previous reports on synthetic systems, and the analysis here sheds additional light on potential charge transport changes. Significantly, a key finding is that there are two different mobility mechanisms for ion transport depending on hydration.

Supplementary material for this article is available online

Keywords: BSF/melanin, hydration, mobility, circular economy

1. Introduction

There are several interlocking societal challenges that require urgent attention including medical sensing & treatment, the ubiquitous sensing network, electronic waste (e-waste) and the need for a circular economy [1, 2].

Medical sensing & treatment is foremost on the mind of governmental bodies, e.g. the United States National Academy of Engineering has elucidated the need for 'advance health informatics' among its 14 grand challenges for engineering in the 21st century [3]. This interest is shared by the pharmaceutical industry, which have coined the term 'electroceuticals', a medical field focused on using electrical signals to affect a medical outcome [4]. Consequently, a rapid growth in research is being experienced in the field of bioelectronics, a field at the

* Author to whom any correspondence should be addressed.

intersection of the physical, chemical and life sciences that is investigating new types of medical sensors [5, 6].

This need for sensors is shared more generally in the concept of the ubiquitous sensor network, the goal of which is to seed the environment with low end sensing devices to monitor variables such as pressure, temperature, humidity etc [1] to enhance control and understanding over a local environment.

However, the above need and use for various sensors will lead to an increase in e-waste, which is already a significant problem due to both the sheer volume of waste generated (45 megatons per year) and the environmentally hazardous materials involved [1]. One method to manage e-waste, and indeed waste problems in general, is to adopt a circular economy approach in which recycling plays a major role [7].

Clearly, materials will need to be selected that have desirable sensing properties but can also be sustainable sourced. Furthermore, once used, disposal must lessen environmental impact. As such, biomaterials are key to this endeavour [8]. They offer the best potential in the matrix of needs of sensing properties, biocompatibility, easy disposal, and being readily sourced.

One biomaterial of great interest is the pigment eumelanin, nature's brown-black pigment [9, 10]. This stacked oligomer polymeric system is synthesised from two main monomers: 5,6-dihydroxyindole (DHI) and 5,6-dihydroxyindole-2-carboxylic acid (DHICA) [11] Eumelanin has a number of unique physical and chemical properties [12–14] such as broad band optical absorbance [15], metal ion chelation [16–19], paramagnetism [20], radiation protection [21], and humidity dependent conductivity [12, 22, 23] just name a few. Eumelanin's natural biocompatibility (it is synthesised *in vivo*) has made it attractive and many promising devices [24, 25] and applications have already been tested, e.g. pH sensing [26], transistor devices [22], capacitive components [27–29] and optical coatings [30].

Eumelanin is a potential 'work horse' material candidate but it cannot be readily sourced. Usually, one can synthesise the material [12], which runs counter to the ideals of a circular economy or source it from animals such as the cuttlefish [31, 32]. The latter results in a limited supply since it is a seasonal by-catch and has low yields due to the cuttlefish emptying their sacs when caught.

A second problem is that eumelanin is not readily processed, and is notorious for its insolubility in water and common solvents [9]. But now, the ability to produce, in bulk, a water-soluble eumelanin has been recently produced from the pupal exuviae of the black soldier fly (BSF) (*Hermetia illucens*) [33], an insect which is rapidly being utilised to metabolise and upcycle food waste [34, 35]. As such, this source of eumelanin is poised to address the aforementioned drawback of eumelanin. A key question regarding this BSF eumelanin (BSF-mel) is whether it retains the desirable properties of eumelanin, especially its electrical properties. Furthermore, can this form eumelanin elucidate the still outstanding scientific questions regarding the origins of the electrical properties of eumelanin? The purpose of this current work is to investigate the electrical properties of BSF-mel. Since eumelanin is known to exhibit mixed ion/electronic conduction [23] and have a hydration dependent conductivity [12, 22, 36], we perform AC conductivity/dielectric spectroscopy on BSF-mel drop-cast films on interdigitated electrodes (IDEs).

The key to the study is that we perform *in-situ* hydration-controlled experiments, utilizing both H_2O and D_2O vapours to tease out the electrical response, the first for a natural based eumelanin compound. We further analyse the data in-depth and compare the results to what is known from synthetic samples and discover intriguing differences that extend the current understanding of charge transport in eumelanin compounds.

2. Materials and methods

2.1. Eumelanin extraction

BSF-Mel powders were provided by the manufacturer INSECTTA Pte. Ltd for on-demand, basic research purposes and used as is. The material is produced via a patented [33] targeted extraction process from the BSF (*Hermetia illucens*).

Briefly, pupal exuviae were homogenised into ∼0.5 mm pieces and demineralised with 10% (w/w) lactic acid for 3 h at 25 °C. The solid fraction was deproteinated with 1 M sodium hydroxide for 3 h at 50 °C. Following this, BSF-melanin was liberated from the solid fraction by heating with 2 M sodium hydroxide for 3 h at 90 °C. The pH of the supernatant was corrected to 1 with 37% (v/v) hydrochloric acid, in order to precipitate BSF-melanin, which was collected by centrifugation and further subjected to a series of proprietary steps in order to derive a lyophilised, salt-free, water-soluble powder. The latter property is achieved at pH 7.3, lower than a standard synthesis pH of 8.

Sample variation from extraction was quantified by UV-Vis spectra of several batches and shows a consistent, reproducible product (see figure S0).

2.2. Thin film deposition

Solutions of BSF-Mel were prepared by stirring in deionized water at a concentration of (20 mg ml^{-1}).

Thin films were prepared from approx. 10 μl of the solution via drop casting deposition and left to dry in a fume hood at room temperature for several hours. For the electrical measurements, Ti/Au IDEs substrate were used, supplied by MICRUX (Ti/Au thickness, 50 nm/150 nm). Two IDE configurations were employed: a linear configuration (120 finger pairs, 10 μm width, 10 μm finger gap, figure 1 top left) and a round configuration (90 finger pairs, 10 μm width, 10 μm finger gap, figure 1 top right). Relative size of IDE can be seen in figure 1, bottom. Before the drop casting procedure, the IDEs were treated by UV-Ozone (Ossila Ltd) for 5 min.

2.3. BSF-mel device preparation and impedance measurements

We performed two sets of environmentally controlled measurements on BSF-Mel by utilising a JANIS Research Cryogen

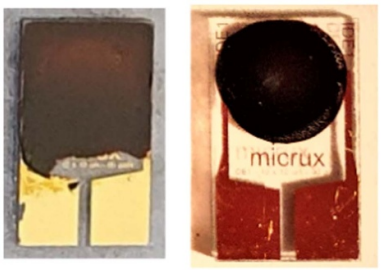

Figure 1. BSF-mel layer dropcast on a linear (top left) and round (top right) IDE at a concentration of 20 mg ml^{-1}.

Free Micromanipulator probe station with an attached vapour delivery system. The JANIS was initially pumped down to a vacuum of $\sim 10^{-2}$ mbar utilising a dry scroll pump. The samples were then exposed to selected values of vapour pressure of H_2O or of D_2O from a vial of liquid (degassed). The basic approach has been described elsewhere [23, 37, 38] but in brief, after the initial pump down, the water vial is opened, and water vapour is bled into a delivery line until a target vapour pressure is read off the pressure gauge (Edwards GK series 0–50 mbar). The samples were then allowed to come to equilibrium (1 h, monitored via electrical impedance spectroscopy (EIS) measurement), electrical measurements were then performed, and the above procedure then gets repeated at a higher vapour pressure until a complete isotherm is obtained. The range of temperatures for the experiments were 20.6 °C–22.0 °C. The vapour pressures obtained were converted into relative humidity accounting for the temperature. This allows for estimating the saturation vapour pressure via Antoine parameters [39].

EIS was performed by using an automated Metrohm Autolab potentiostat PGSTAT302N with a FRA32M module. The AC voltage amplitude, V_{AC}, was fixed at 300.0 mV and the frequency (f) range was 1.0 MHz—0.1 Hz, taking 10 data points per decade—and the DC offset was 0 V.

2.4. Impedance data analysis

The EIS spectra of impedance (Z) vs f have been represented in multiple formats. The first employs a Nyquist plot (NP) i.e. the negative imaginary component of the impedance (–Im Z) vs. the real component of the impedance (Re Z). We recall that in a NP the left component of the data set refers to the high frequency region while the right part to the low frequency region [40]. The data is then modelled by building up an equivalent circuit that replicates the shape of the data via a combination of resistive (R), pure capacitive (C), peculiar impedances components such as the constant phase (Z_{CPE}) and diffusion (Z_W) elements (see ESI) to represent the AC electrical response [40]. Each circuit element can be assigned to a specific mechanism depending on the AC frequency signal range under consideration.

To analyse data in a NP, we adopted the free downloadable EIS Spectrum Analyzer v.1.0 software [41]. The equivalent

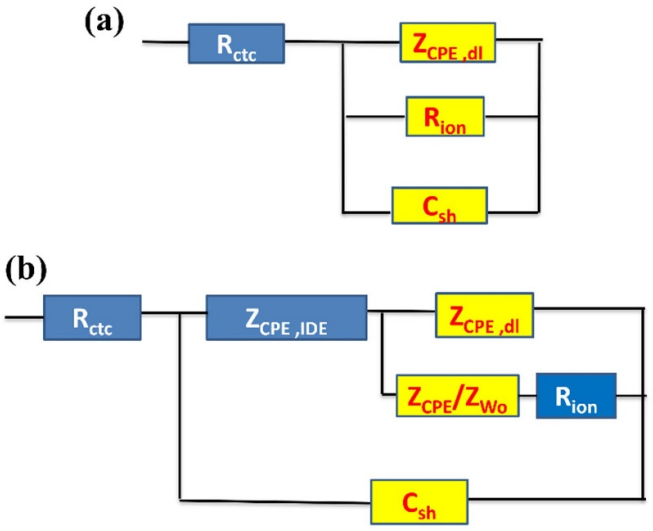

Figure 2. Equivalent circuits adopted for the best fitting of the experimental NPs data (see figure 3 below) on BSF-mel layers. The best fit parameters have been summarized in table S1 in the ESI. The circuit in (a) refers to the NPs obtained at the lower relative humidity values of D_2O and H_2O; (b) scheme of the circuit adopted for all the other values of vapor pressures for both solvents; a Z_{CPE} was used at the highest values of D_2O or H_2O vapor pressure instead of a Warburg element to capture electrode polarization effects.

circuits employed herein are depicted in figure 2. The two different circuits shown represents two different regimes, which we will discuss separately.

Figure 2(a) is for drier BSF-Mel, i.e. either to D_2O at 18% RH or H_2O at 20%RH. The circuit consists of the Ti/Au contact and other IDE component resistances represented by R_{ctc}, the shunt IDE capacitance C_{sh} is present to simulate the parasitic current shunts at high frequency [42], and the electric double layers at the interface with the electrodes is simulated by a non-ideal capacitance, i.e. a constant phase element ($Z_{CPE,dl}$). No additional diffusive Warburg element was used as it did not significantly improve the fit.

Figure 2(b) was applied to both wet D_2O (30%–97% RH) and H_2O (28%–92% RH), where an embedded Randle circuit was employed, which is particularly suitable for simulating carrier transport mechanisms in electrolytes placed in between two electrodes [43]. The Randle circuit commonly consists of a resistor (R_{ctc}, the contact resistance) placed in series with two branches in parallel: the first branch is constituted by a constant phase element ($Z_{CPE,dl}$) or a capacitor (C_{dl}) representing the charge double layer (dl) forming at the electrolyte/electrodes interface; the second branch refers to the faradaic current and is constructed by two elements in series, which are the charge transfer resistance or ionic charge resistance R_{ion}, and an impedance associated to the charge diffusion (Z_W). To improve fitting, the Randle circuit is sometimes rebuilt by introducing a Z_{CPE} or a specific Warburg Element depending on the behaviour at low frequency (Z_{CPE}/Z_{wo}, figure 2(b)). In particular, the Randle circuit was modified by substituting the Warburg impedance Z_W with the more appropriate diffusion element, Warburg finite length, (Z_{Wo}), given by:

$$Z_{Wo} = \frac{A_W}{\sqrt{i\omega\tau_D}}\coth\sqrt{i\omega\tau_D} \tag{1}$$

$$\text{with } \tau_D = \frac{\delta^2}{D} \tag{1a}$$

where A_W is the limited diffusion resistance, D the diffusion coefficient of the electroactive species and δ the Nerst diffusion layer representing a carrier finite-length diffusion with electrode reflective boundary [44–46]. Z_{Wo} is an element that can be expressed via a complex number (equation S6) and both real and imaginary components can be expressed to be proportional to $1/\sqrt{\omega}$ and also $\sim D^{1/2}/\delta$, following the approaches of other authors for the absorbing element [41, 46, 47] In the low frequency limit the real part W_{Or} is proportional to the diffusion resistance and the imaginary component W_{Oc} is proportional to $1/\sqrt{\omega}$ and $\sim D/\delta^2$ (equation S9 & S10). This Randle circuit was then placed within our larger IDE, to which we have also added the $Z_{\text{CPE,IDE}}$ and C_{sh} terms. The former characterizes the surface roughness at the electrode/electrolyte interface and the latter the parasitic current shunts at high frequency [41] Notably, the appearance of a $Z_{\text{CPE,IDE}}$ at high hydration levels is also contributing to the appearance of electrode polarization (EP) at high hydration levels together with the increase of the $Z_{\text{CPE,dl}}$.

The second way of analysing the EIS data was done via the broadband dielectric spectroscopy (BDS) approach. BDS was performed by the comparative study of the complex dielectric permittivity ε^* and the complex AC conductivity, σ^* [40]. This approach allows understanding by inspecting data in the frequency domain. The complex permittivity ε^* is expressed by the real ε' and imaginary part ε'' of the permittivity as in the following equation (equation (2)):

$$\varepsilon^* = \varepsilon' - i\varepsilon'' \tag{2}$$

where ε' and ε'' represent the storage and loss part respectively and is calculated by using the Re (Z) and Im (Z) frequency dispersions following the classical expressions [40]:

$$\varepsilon' = \frac{-\text{Im}Z}{2\pi f|Z|^2 C_0}; \quad \textit{and} \quad \varepsilon'' = \frac{-\text{Re}Z}{2\pi f|Z|^2 C_0} \tag{3}$$

with C_0 the equivalent geometrical vacuum cell capacitance (i.e. no sample between the electrodes) and with $|Z|^2$ the modulus squared of the impedance Z.

In the present case the value for C_0 is taken to be the value measured at high frequency for our empty IDE, namely 20 pF for the linear and 10 pF for the round geometry. We also determined the loss factor via [48, 49]:

$$\tan\delta = \frac{\varepsilon'}{\varepsilon''} \tag{3a}$$

which is useful for determining the ratio between the dissipative and dipolar component of the system under test. The Trukhan model is adopted here as a preliminary estimate of the free ion charge diffusion coefficient D via the expression:

$$D = \frac{\omega_{\max} L^2}{32(tan\delta_{\max})^3} \tag{4}$$

with L being the distance between the electrodes and $\omega_{\max}$ being the angular frequency at which $\tan\delta$ is a maximum. In the present the value for L we take as the distance between each pair of fingers i.e. 10 μm.

The values for $\tan\delta_{\max}$ are related to the Debye length [50], i.e. the distance of the occurrence of the charge screening effect with respect to the applied electric field

$$L_D = \frac{L}{8(\tan\delta_{\max})^2}. \tag{4a}$$

The free ionic charge concentration n and mobility μ are given by:

$$n = \frac{\sigma'(\omega_{\max})_{\text{AC}}}{D} \times \frac{k_B T}{e^2} \tag{4b}$$

and

$$\mu = \frac{\sigma'(\omega_{\max})_{\text{AC}}}{en} \tag{4c}$$

where $\sigma'(\omega_{\max})_{\text{AC}}$ is the real part of the AC conductivity at $\omega_{\max}$. This corresponds to the centre value of the σ'_{AC} plateau. Continuing, k_B is the Boltzmann constant, T the temperature and e the electronic charge of 1.6×10^{-19} °C. Here we consider the room temperature values, thus $k_B T = 0.025$ eV.

The complex AC conductivity σ^* is determined via the $\varepsilon^*(\omega)$ using the expression [40]:

$$\sigma^*(\omega) = \sigma'(\omega) + i\sigma''(\omega) = i\omega\varepsilon_0\varepsilon^*(\omega) = i\omega\varepsilon_0\left(\varepsilon' - i\varepsilon''(\omega)\right). \tag{5}$$

The radial frequency dependence of $\sigma^*(\omega)$ was discussed considering the radial frequency functional dependence:

$$\sigma^*(\omega) = \sigma_{\text{DC}} + A\omega^n + B\omega \tag{6}$$

i.e. in the framework of the Jonscher's classical power $(0 < n < 1)$ and Funke approach $(n > 1)$ [51] and by the addition of a third term representing the nearly constant loss term (NCL) [52]. Here σ_{DC} is the DC ionic current, $A\omega^n$ refers to AC conductivity whose mechanisms will depend on the resulting n values and B is the slope of the linear growth of the conductivity. Typically, for $0 < n < 1$ we will refer to a conduction mechanism governed by ionic charge jumps due to translational motion with hopping from delocalized states, whereas for $n > 1$ the hopping occurs between localized states. The AC permittivity experimental data were fitted using Novocontrol WinFIT 2.0 software allowing to insert up to three relaxation peaks described by the Havriliak–Negami (HN) model. The HN model is generally used to model BDS data showing more

than one relaxation time distribution. It is, alongside an additional conductivity term, expressed as follows:

$$\varepsilon^* = \sum_{j=1}^{K}\left[\frac{\Delta\varepsilon_j}{\left(1+\left(i\omega\tau_j^{a_j}\right)\right)^{b_j}}+\varepsilon_{\infty j}\right]-i\left(\frac{\sigma_{\mathrm{DC}}}{\omega\varepsilon_0}\right)^N \quad (7)$$

where the *j*th dielectric relaxation function is summed into a superposition. Each function is characterized by a relaxation time distribution peaked at a specific time (τ_j) with characteristic parameters a_j, b_j, $\varepsilon_{\infty j}$ and $\Delta\varepsilon_j$, the latter of which is termed the dielectric strength and proportional to the area below the *j*-relaxation time distribution. The parameters a_j and b_j refers to the symmetry and broadening of the time relaxation distributions. If $b_j = 1$ and $0 < \alpha_j < 1$, the HN distribution is symmetric and it reduces to the 'Cole–Cole' distribution (C–C) whereas with $a_j = 1$ and $0 < b_j < 1$, the HN function is an asymmetric distribution termed the 'Cole–Davidson' distribution (C–D). The last term is construed of the ionic DC conductivity σ_{DC}, the permittivity of free space ε_0 and N. This last term adds to the dielectric loss at low frequency due to DC ionic conductivity with N regulating the slope of the straight line underlining the extension of the EP [53–56].

The set of best fit parameters (a_j, b_j, σ_{DC}, N) were afterwards used for the calculation of each HN*j* $j = 1,2,.\ K$ here $K = 3$) functions and their superposition leading to the permittivity curve that best fits the experimental data [57]. Finally, we determine the frequencies of the maximum of each loss component of a HN function via [57]:

$$f_{\mathrm{MAX,HN}j} = \frac{\omega_{\mathrm{MAX,HN}j}}{2\pi} = \left(\frac{\sin\left(\frac{\pi a_{\mathrm{HN}j}}{2(b_{\mathrm{HN}j}+1)}\right)}{\sin\left(\frac{\pi b a_{\mathrm{HN}}}{2(b_{\mathrm{HN}j}+1)}\right)}\right)^{a^{-1}}\tau_{\mathrm{HN}j}^{-1}. \quad (8)$$

3. Results and discussions

3.1. EIS analysis via Nyquist plot

The exposure to H_2O and D_2O vapours modify the features of the electrical response as depicted in figure 3. Starting from the dry regime, both sets of results display a pronounced circle corresponding to a high impedance value; under increasing the vapour exposure, the NPs progressively start to manifest a Randle circuit-like response. Corresponding changes in the modelled components, R_{ion}, Z_{W0} and C_{dl} also occur, but values depend on whether it is H_2O or D_2O vapour exposure. It is noteworthy that in the low frequency region the impedance of a BSF-mel film is higher for D_2O exposure rather than H_2O, as can be derived by the corresponding wider semicircle observed [58], thus suggesting a lower ionic conductivity when exposed to D_2O. These results agree also with those observed on cephalopod proteins [58].

Additionally, we discount a significant electronic component to the electrical response for two reasons. Firstly, The NP analysis for the simplest circuit discounts the use of an additional parallel resistance, usually employed for electrons. Indeed, for the diffusion tails that are seen, if electrons are present, one would expect curvature back towards the real axis at low frequency. Secondly, as can be seen in the conductivity and dielectric spectra below (figure 5), the qualitative shapes of the curves are representative of ionic systems [59]. Specifically, there is an electrode polarisation regime at low frequency, a flat real conductivity/plateau in an intermediate frequency range indicating diffusion control and then a power law dependence of the real conductivity at high frequency. These trends hold across the hydration range.

The full set of the best fit parameters have been summarized in the table S1 in the ESI. Focusing on the R_{ion} parameter, we found the values under D_2O exposure were larger than for H_2O exposure at similar humidity values (see figure 4) [23]. The trend line also shows a decrease of four orders of magnitude from low RH to high RH. We recall that in a Randle-type circuit, the R_{ion} resistance is usually associated to the faradaic current R_{ct} when applying a redox potential [60]. However, a faradaic current's origin is usually due to redox processes, that is referenced relative to a reference electrode. In our case, our approach is much simpler, and we only apply a softer 0.0 V DC offset. As such, we assume that R_{ion} represents actual ionic current, then under H_2O we have a higher ionic current relative to D_2O vapour exposure [60]. Whether this is driven by ionic concentration changes or mobility changes, is further explored in the discussions below.

The term assigned to the charge double layer ($Z_{\mathrm{CPE,dl}}$) forming at the electrodes has for D_2O exposure, has a value independent of RH ($n \sim 0.6$)), being closer to a capacitor, whereas for H_2O exposure n increases from ~0.6 to ~0.8 with RH (see table S1). The W_o element has a peculiar behaviour depending on D_2O or H_2O exposure. Given the order of magnitude of the values extracted for the real and imaginary components (table S1), it is consistent with equation S9, i.e. low frequency limit. In this limit, the real part related to the Warburg diffusion impedance decreases in both cases. This is in essence additional evidence for enhanced ionic conductivity as expressed in figure 4. Conversely, the term related to the imaginary part is increasing with RH for H_2O exposure and decreases for D_2O exposure. A few situations may account for these behaviours. It could be that the width of the Nerst diffusion layer expands under D_2O and shrinks under H_2O, thus implying a greater increase in charge concentration near the electrode under D_2O than under H_2O. This is represented at the highest RH by a ZPE element $Z_{\mathrm{CPE},n3}$ replacing the W_o one in both cases, with the n ~ 0.9 in D_2O i.e. a more capacitive element, respect to the more diffusive one in H_2O where $n = 0.5$ (table S1). On the other hand, the different behaviours for the imaginary component may be due to a decrease in the diffusion parameter for D_2O (i.e. lower mobility) than under H_2O (i.e. higher mobility). Of course, it may be that it is a combination of the above. This requires further interrogation, which is the purpose of the next set of analyses.

3.2. BDS data analysis

3.2.1. Frequency dependent complex spectra. The real and imaginary part of the dielectric permittivities, ε' and ε'' respectively, and conductivities, σ' and σ'' respectively, of the

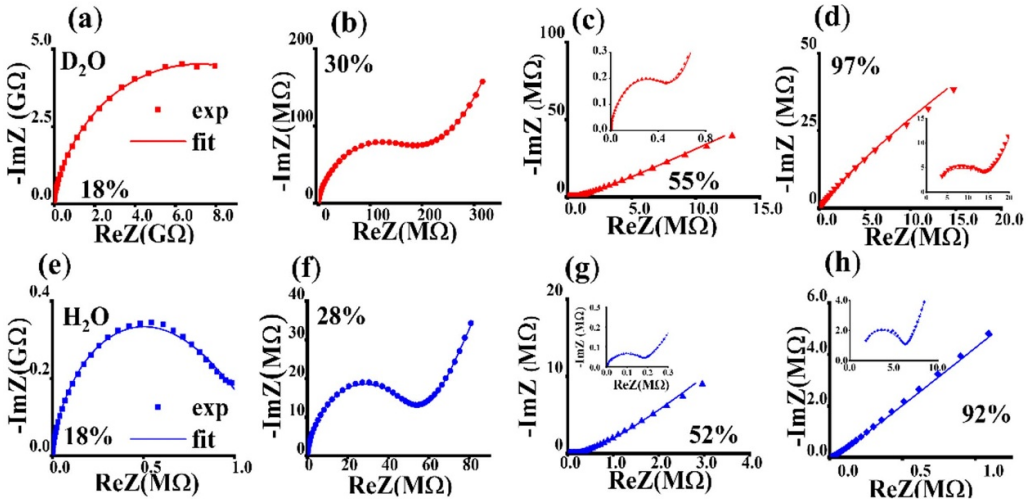

Figure 3. NP representations of a BSF-layer on a linear IDE under exposure of D_2O (red curves, upper column) and H_2O (blue curves, lower column). Relative humidity are expressed as RH (%). The insets are the magnified views of the NPs in the high frequency region. Similar behaviors were observed on IDE round geometries (figures S1 and S2 in ESI).

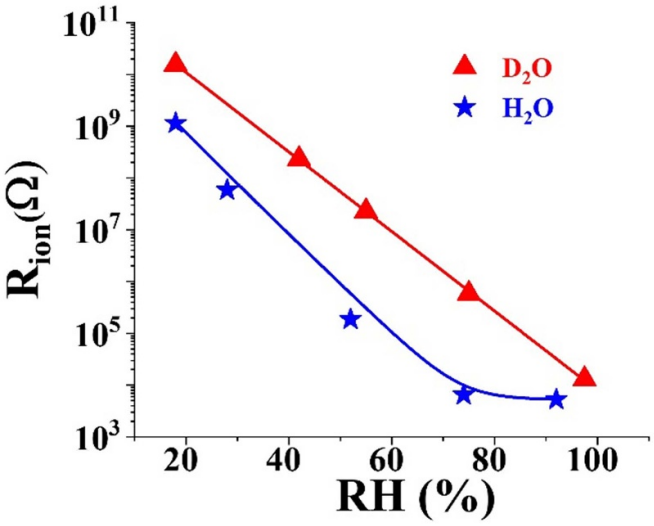

Figure 4. R_{ion} vs. RH (%) based upon the best fits to the NPs circuit (c) in figure 2. Depicted are the D_2O (red triangles) and H_2O (blue stars) data sets. The colored lines are the best fits using an exponential decay function, $R_{ion} = R_{ion,0} + A\exp(-RH/RH_0)$ where RH_0 is a 'decay constant' with values of 5.8% for D_2O and 4.1% for H_2O.

BSF-Mel layers exposed to H_2O and D_2O are displayed separately for two RH regimes (low and high) in figure 5. Note, low and high regimes are only loosely connected to that of the NP analysis. The reason behind this choice is due to the dielectric spectral features displaying a substantial modification for RH values higher than ∼40% for both vapours, hinting at modification in the ion transport mechanisms due to hydration.

The dielectric features in figure 5 are progressively evolving with RH and is replicating to a certain extent that has been already observed for synthetic melanin [23], with the additional advantage of our frequency range being lowered down to 0.1 Hz, enabling an enhanced range to investigate ionic charge dynamics. The increase in RH causes a development of a plateau at low frequency in ε' and a sharp increase of σ' up to a plateau underlining the extention of the EP with hydration. This behaviour is similar in fashion to what is observed in ionic polymer electrolytes or ionic liquid when increasing the temperature [49, 61–64], which implies a similar action between temperature and hydration as environmental variables [22].

Turning to the RH range of ∼20%–∼40% (figures 5(b) and (f)), the real part of the conductivity follows the Johnsher's power law ($n < 1$), evidencing a non localized hopping regime. The frequency extention of this power law depends on the hydration level, which is then followed by a NCL region, i.e. $n = 1$. The hopping regime is characterized by n values of 0.6–0.5 under H_2O and 0.7–0.6 under D_2O exposure. As described in the methods section, values closer to $n = 1$ suggest a higher charge localization; therefore we infer that the larger values for n under D_2O is a hint of more charge localization vis-à-vis H_2O, maybe due to a higher energy barrier of formation [51]. In the same RH regime, the ε' curves show a tail and a kink with increasing RH at the low frequency region, the former ending with a plateau corresponding to the value of the static dielectric constant ε_R. at high frequency.

In the RH regime of ∼50%–∼95%, the real part of the AC conductivity (figures 5(d) and (h)) displays a sharp increase ending with a plateau and the tail of the NCL region whose onset progressively shifts toward frequencies higher than 0.1 MHz. The best fit of σ' to equation (6) returned values of n larger than 1.0, which following the Funke theory [51], suggests that the jump relaxation occus between localized states. This observation should be noteworthy, as it suggests that there may be some qualitative change in the charge structure of melanin with increasing hydration. The sharp increase in σ' corresponds to the plateau in ε' and together with σ'' behaviour and progressively appearing of ε'' bumps, marks the frequency extention of the EP. It is noteworthy the wider frequency extension of the EP region in the case of D_2O relative

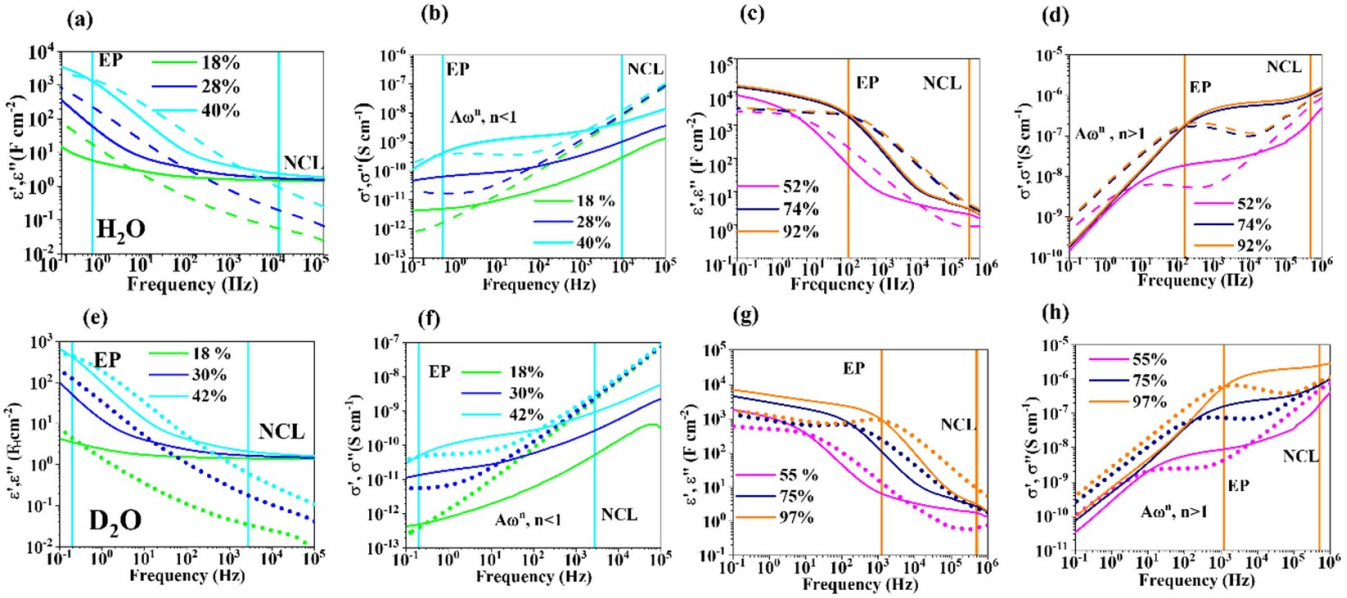

Figure 5. Real (solid lines) and imaginary (dotted lines) parts of the complex dielectric permittivities (a), (c), (e), (g) and the corresponding complex conductivities (b), (d), (f), (h) of the BSF-mel layers. The data is organised by exposure to H_2O (upper row) and D_2O (lower row) in the low (a), (b), (e), (f) and high (c), (d), (g), (h) RH regimes. The cyan vertical straight lines are representative of the frequency of the electrode polarization (EP) and nearly constant loss (NCL) at RH = 40% and 42% whereas the orange lines refer to those of the EP and NCL at RH = 92% and 97.5% for H_2O and D_2O respectively.

to the H_2O exposure data set, which is consistent with the idea of an increase in the Nerst diffusion length as discussed under the NP analysis. As such, we suggest that this analysis of the complex permitivity and conductivity data would imply that the underlying reason for the qualitative difference in the complex component of the Warburg element was due to a greater rate of expansion of the Nerst diffusion layer relative to the diffusion constant. As to the latter quantity, it will be explored below.

3.2.2. Permittivity best fit via HN modelling and underlying polymer dynamics. The dielectric permittivities at selected RH values have been fitted using the HN formalism (equation (7)). The full set of the best fit parameters are summarized in the ESI, table S2. Example fits can be seen in figure 6. The assignement of each HN peak to a corresponding relaxation processes was done either by depending on the permittivity behaviour, or by making a comparative analysis with the AC conductivity (figure 5). In the range of ∼20% to ∼40% RH (both vapours) we see at RH 20% and 30% a contribution from the permittivity relaxation at high frequency corresponding to the regime where the Jonscher's hopping region transitions to the NCL, which we will label as HN_{NCL} in the ESI. At ∼40% the EP is captured (HN_{EP}) at an oscillator frequency of 0.2 Hz and 0.5 Hz (D_2O and H_2O respectively) In the conductivity, this correspond to the starting of the Funke regime (visible as a short straight line in the region 0.1 Hz–1.0 Hz, figures 5(b) and (f)) still followed at higher frequency by the Jonscher's hopping one. At these intermediate RH values, the dielectric strengths ($\Delta\varepsilon$) for HN_{EP} and HN_{NCL}, differ about three orders of magnitude. A peak at 0.2 Hz was already observed for similar hydration levels in HN_{EP} but no equivalent to the HN_{NCL} was modelled, although the latter is a feature often observed in ionic conductors [52, 63, 65].

Representative complex permittivity spectra results for the RH range from ∼50% to ∼100% and HN best fits are shown in figure 6 for a sample on a linear IDE (example used at 70% RH), with tables S2(a) and (b) (ESI) summarizing the full set of best fit parameters. The complex permittivity spectra evolves in a fashion like that observed in a variety of structures seen in many polyelectrolytes or ionic conducting membranes, when increasing the temperature [61, 62, 66–69]. Therefore, we opt to interpret the dielectric behaviour in BSF-mel in a similar fashion, but using RH instead as the independent environmental variable. The data was modelled by the superposition of three HN functions. First of all, no peak was assigned to the NCL/hopping transition region as it was found to progressively move to higher frequencies and out of our measurement range (see figure 5). Given that the dielectric behaviour of BSF-mel have similarities with those seen in ionic conducting polymers, we assigned the other three peaks as the α and β relaxations, which relate to the inner polymer structures, and the highest frequency to electrode charging, i.e. HN_{EP}.

Generally in pemittivity spectra, both α and β relaxations are due to the formation of polymeric chains whose aggregate dimensions and distances are modified during hydration and deuteration, which then change the 'polymer' chain aspect ratio [69]. In this particular case, we venture to attribute the lower frequency α-relaxation to chain diffusion in the hydrated/deuterated BSF-Mel polymer whereas the β-relaxation is associated with polymer structures that can be associated with the diffusion from hydronium/dihydronium

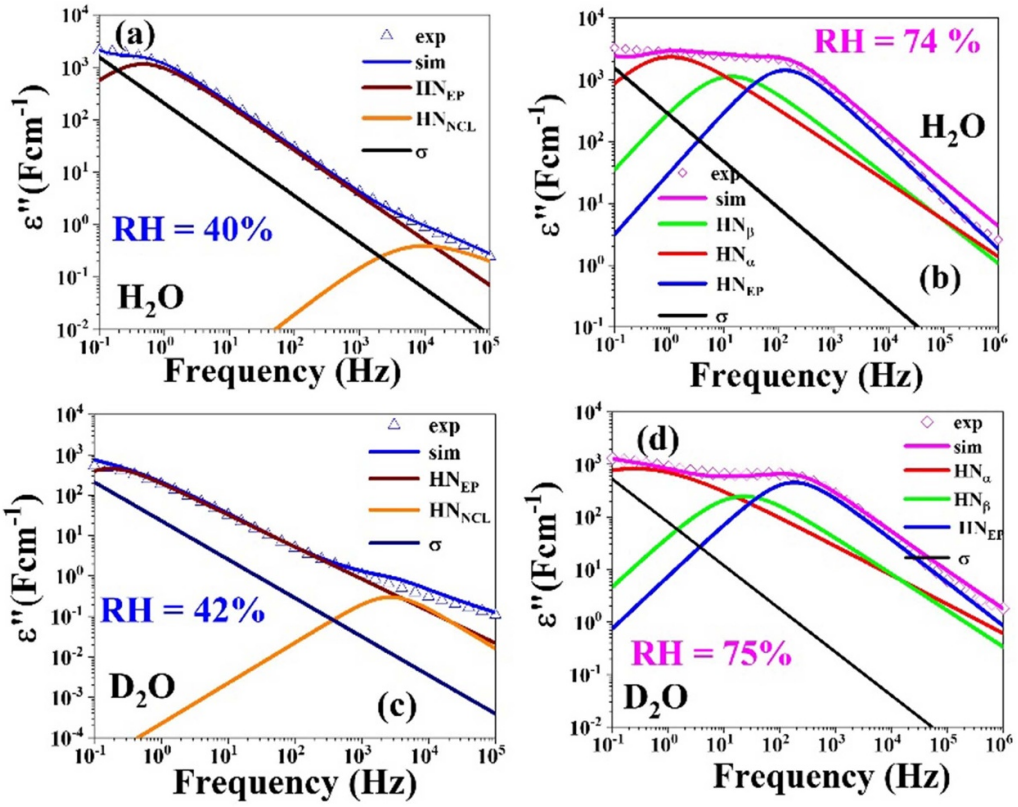

Figure 6. Experimental dielectric losses ε'' vs. f (triangles and diamonds in the low and high RH regimes, respectively) for a representative BSF-mel layer on a linear IDE under similar increasing values of the H_2O and D_2O relative humidities. Best fit cuves, $HN_{\alpha,\beta,EP}$ functions and the linear conductivity term labeled with σ @ $\left(\frac{\sigma_{DC}}{\omega\varepsilon_0}\right)^N$ are also depicted as solid lines. See tables S2(a) and (b) in ESI for fitting parameters.

ion hopping mechanisms. One can relate the α and β relaxations peak frequencies ($f_{\alpha/\beta,MAX}$) to a diffusion coefficient (D) via [69, 70]:

$$f_{(\alpha/\beta),MAX} \propto \frac{D_{\alpha/\beta}}{l^2}$$

with $D_\alpha = D_{chain}$ being for the chain diffusion for the α–relaxation and l the radius of gyration R_g of the chains. For β-relaxation, it implies that smaller aggregates have a diffusion of $D_\beta = D_{aggrepate}$ and l the distance between the aggregates. The observed blue shifts in f_α and f_β when increasing the RH (see figure 7) hint respectively at the reduction of the aggregate radius (α-relaxation) and the distance for aggregate movement (β-relaxation), implying a coalescence of progressively smaller aggregates in a continuous layer [69, 71–73] and/or an increase in the diffusion coefficients

The dielectric strengths $\Delta\varepsilon$ (see table S2 ESI) of the α-relaxations display a slight increase both under H_2O and D_2O exposure whereas in the β ones it increases in D_2O and is almost constant in H_2O, which may be a consequence of deuteration of the polymer backbone.

The maxima f_{EP} for the HN_{EP} also display a blue shift vs. RH (figure 7). We recall that the f_{EP} represent the frequency of the fully developed EP, whereas the frequency of the maxima in the loss factor (equation (3)) refers to the start of the EP. Both this frequency and loss factor are reciprocally related to the Debye length L_D. Therefore, one can infer that L_D decreases with increasing RH.

The dielectric stength $\Delta\varepsilon_{EP}$ were also found directly related to the f_{EP} and to the double layer capacitances (see figure S4),

represented by the $Z_{CPE,dl}$. The peak frequency f_{EP} and $\Delta\varepsilon_{EP}$ were lower in the case of D_2O exposure vis a vis H_2O. The former hints that in the case of D_2O the slower response (low f_{EP}) is likely to be due to the higher mass of deuterated hydronium ions whereas the latter can be explained as due to the lower ion concentration, n_{ion}, of D_2O free ionic charges.

3.2.3. Trukhan modelling and ionic charge concentration and mobility extraction. Overall, the values of σ' at the plateau in AC measurements are considered the DC conductivity values. In our case we obtain the value at the frequency of the maximum of the loss factor (see figure S2 in ESI). For the full RH range it can be seen (figure S6) that the conductivity ranges between 10^{-11} S cm^{-1}–10^{-5} S cm^{-1} under D_2O exposure and from 10^{-10} S cm^{-1}–10^{-6} S cm^{-1} under H_2O exposure, in line with previous observation on thin films of synthetic melanins [23, 74]. These observations are also consistent with the 4–6 orders change in the ion resistance as discussed under the NP analysis.

To investigate the charge transport properties further, we employ the methods of Trukhan, which thus far has not been employed on these materials. The advantage of this approach

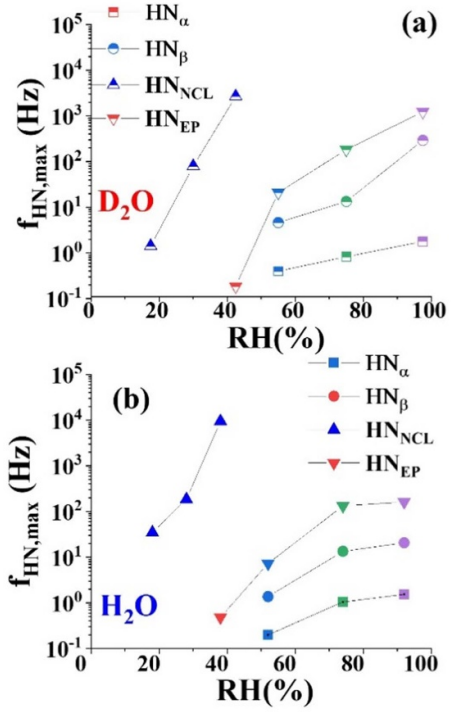

Figure 7. Values of the peak frequencies of the various HN peaks as a function of RH of D_2O (a) and H_2O (b) exposure of the BSF-mel. Each symbol refers to a specific HN function: triangles for NCL relaxation (HN_{NCL}); squares for α-relaxation (HN_α); circles for β-relaxation (HN_β); inverted triangle for EP (HN_{EP}). The increase of the peak frequency vs RH (same colors of the symbols for similar RH ranges) indicates a blue shift for all the relaxation processes.

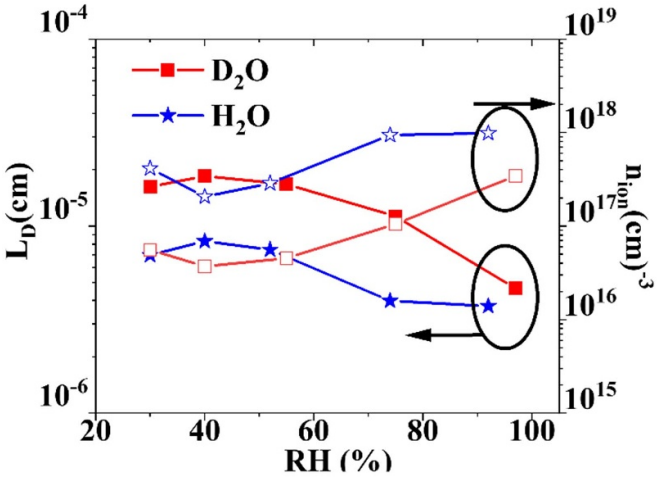

Figure 8. Debye lengths L_D (left) obtained from equation (4) and free ion charge concentration (right) obtained from equation (4) as a function of RH for BSF-mel on a linear IDE. Solid symbols represent the Debye length and open symbols the charge concentration. Red data is for D_2O exposure and blue data for H_2O exposure.

is that it will allow potential insights into the mobile charge concentration and mobility, which has been noted as sorely needed to advance understanding of these polyindole quinone materials [12, 36, 38, 75].

The first step in the analysis is to obtain the Debye lengths L_D, which were obtained via equation (4) and is depicted in figure 8. These lengths scales were found to be systematically larger under D_2O exposure versus H_2O, with both vapours leading to a decrease with increasing RH. Notably, such a change in the Debye length is again commonly observed in ionic conducting polyelectrolytes when increasing temperature [50]. As above, such a similarity suggests that in melanin the RH has a role equivalent to temperature [22].

Using equation (4) the ion concentration n_{ion} was calculated (figure 8 and table S2). The data show that the ionic charge concentration and conductivity increases with increasing RH, in-line with previous interpretations where it is expected that

dissociation of carboxylic acids [75] and protonated semiquinones from a comproportionation reaction would supply protons for conduction [74, 76]. What is striking is that the charge concentration for BSF-mel is systematically higher under H_2O exposure than for D_2O exposure, but the rate of increase is greater under D_2O. This is an interesting result in light of previous work on synthetic melanins [64]. In the work by Rienecker *et al* the rate of the DC conductivity increase with hydration under D_2O was greater than under H_2O, which is also observed in this work (figure S6, ESI). In the aforementioned work the reason given for this different rate of increase was due to a greater generation rate of charges induced by D_2O. This was argued to be due to a systematic shift in the underlying equilibrium chemistry induced by the kinetic isotope effect, i.e. the greater mass of deuterium relative to hydrogen. This initial inference from Rienecker *et al* [64] appears to have been confirmed, as there does appear to be a greater generation rate of mobile charges under D_2O.

Although the IDE geometrical configuration affects the overall order of magnitude of the ion charge concentration and conductivity, the behaviour vs. the RH is maintained (see ESI); as a matter of fact the ratio n (D_2O)/n (H_2O) was found almost to be the same in both device configurations, returning an ion concentration one order of magnitude lower in the case of n (D_2O) in all the RH range. As such, the effect of geometry can be discounted on the qualitative trends observed.

As would be noticed, there is no one-to-one correspondence between the ionic charge concentration and the conductivity. Given this, the mobility of the charges must now be considered, since mobility changes are certainly to be anticipated. The mobility was calculated using equation (4), with the results depicted in figure 9. The first thing of great note is that the mobility changes, both under D_2O and H_2O are ~4–5 orders of magnitude. This would suggest that the primary conductivity change as a function of hydration is driven by the mobility changes, and not by the concentration changes, contrary to the literature of the past decade [12, 76]. These observations also contradict previous work in which muon spin resonance work implied that the proton mobility was constant of the same hydration range [76]. As such, the analysis presented here must be treated with caution. However, this does not mean that the Trukhan approach is not viable, as these previous observations and discussions can all remain true, e.g. the muon particle used in [76] within the time scale observed may

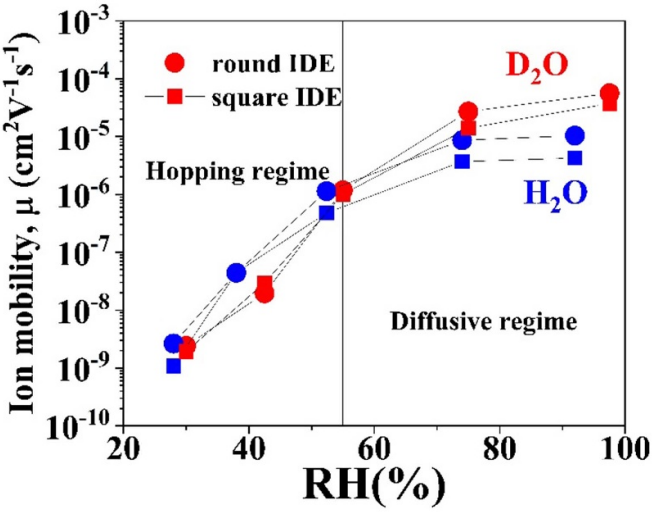

Figure 9. Free ionic charge mobilities μ vs RH for H_2O (blue symbols and lines) and D_2O (red symbols and lines) vapours, calculated by adopting the Trukhan model (see methods section) for a round (round symbols) and linear (squared symbols) IDE geometries.

not be applicable to the frequencies probed in this work. What this situation does highlight is that going forward a major effort on investigating mobility effects must be made. In this framework, it is mandatory to perform a more careful estimate of the ionic charge density, generally requiring a correction factor or its evaluation via other techniques [77].

With caution, we continue and note that there appear to be two ranges for μ *vs.* RH. The first, lower RH regime (0%–50%) show comparable mobility values, maybe slightly lower ones for D_2O vs H_2O, whereas the higher RH regime starts to show a saturation of the mobility and divergence between D_2O and H_2O, with D_2O paradoxically showing a higher mobility.

The low RH regime corresponds to the localised hopping regime in the frequency dependent hopping seen in figure 5, due to the observed $n < 1$. Furthermore, this low regime behaviour is also consistent with the slightly higher power law exponent observed for the D_2O dataset. As for the low RH regime, the high RH regime can be identified alongside the different hopping mechanism that manifests itself as seen in figure 5. Other inelastic neutron scattering [36] and IR spectral studies [75] have noted that there is a qualitative change in water vibrational modes between drier and wetter conditions, which would imply different water structures in the material. Indeed, these authors suggested that a change in mobility may occur and may indeed yield different conductive entities, e.g. hydronium vs Zundel ion. The analysis pursued here do appear to indicate that at the very least we should expect a change in mobility mechanism as melanin is hydrated. The remaining issue is the apparent higher mobility exhibited when exposed to D_2O. One would expect a lower mobility due to the kinetic isotope effect. If the Trukhan model is applicable to these high hydration levels, then the D_2O data is suggesting that whatever the mechanism is for conduction, a standard appeal to mass difference is not going to be sufficient explanation, as the result is opposite to what one may expect. Indeed, a different approach should be considered, maybe along the lines of considering the difference in the Gibbs free energies of H_2O and D_2O and how it affects the energy landscape the ionic entities find themselves in.

Overall, more experimental as well as theoretical work is needed to tease out the mobility mechanism in melanin.

4. Conclusions

A number of key results have emerged from this study. The first is that the hydration dependent conductivity behaviour of BSF-mel is comparable to a number of other works on synthetic melanins, implying similar charge transport properties. The natural advantage the BSF-mel has is its processability and potential upscaling of production, making it a promising sensing material to fit within a circular economy model.

This indepth work has yielded deeper knowledge of the melanins in general [23]. The higher quality data and extensive quantitative modelling, including the Trukhan analysis, has returned new insights into the charge transport mechanism of hydrated melanins. For example, there is a change in mobility mechanism going from low to high hydration states. Furthermore, the data also is consistent and confirms previous inferences as to the behaviour of ionic concentration changes. The double layer capacitances measured at high hydration levels, paves the route for the exploitation of this readily and sustainable sourced biopolymer in a variagate set of bioelectronic applications.

As such, we envisage its implementation as an electrochemical double layer capacitor in batteries and charge storage devices. It may also constitute a suitable and/or gate for organic transistors. Additional data supports this notion given the magnitude and shape of the hysteresis loops (data not shown) and the behaviour seen in the NPs at high hydration. Also, given the humidity dependence, the reactive free radicals sites of the material and physicochemical properties, we envisage sustainably produced humidity and/or other classes of vapor impedance-based sensors. Lastly, by tuning the properties with other components, BSF melanin may be used in biological assays of electroceutical devices. This is particularly relevant given the good biocompatibility of the material [78]. Work on such devices exploiting the high processability of BSF melanin are in progress.

Data availability statement

All data that support the findings of this study are included within the article (and any supplementary files).

Acknowledgments

M A aknowledges the CNR-Short Term Mobility program 2021 Prot.0052594/230721; M A and P F A acknowledge the Italian Ministry of University and Research (MUR)

PONa3_00369 SISTEMA; This work has been funded by Italian Ministry of University and Research (MUR), PRIN MUSSEL- 2017YJMPZN MUSSEL. R G acknowledges the European Union—NextGenerationEU under the Italian Ministry of University and Research (MUR) National Innovation Ecosystem grant ECS00000041—VITALITY—Spoke 9. For A B M: 'This work was also supported by the UKRI Research Partnerships Investment Fund through the Centre for Integrative Semiconductor Materials.'

ORCID iDs

M Ambrico https://orcid.org/0000-0002-0568-6860
A B Mostert https://orcid.org/0000-0002-9590-2124
P F Ambrico https://orcid.org/0000-0002-2455-6949
J Phua https://orcid.org/0009-0002-1763-0861
S Mattiello https://orcid.org/0009-0000-9601-4703
R Gunnella https://orcid.org/0000-0003-4739-6375

References

[1] Puccinelli D and Haenggi M 2005 Wireless sensor networks: applications and challenges of ubiquitous sensing *IEEE Circuits Syst. Mag.* **14** 19–31
[2] Baldé C P, Forti V, Gray V, Kuehr R and Stegmann P International Telecommunication Union (ITU), United Nations University (UNU) & and International Solid Waste Association (ISWA) (Bonn/Geneva/Vienna) *The Global E-waste Monitor 2017: Quantities, Flows, and Resources*
[3] Olson S 2016 National Academy of Engineering *Grand Challenges for Engineering: Imperatives, Prospects, and Priorities* (The National Academies Press) (https://doi.org/10.17226/23440)
[4] Ling G, Lathan C E, Ling G and Lathan C E 2019 Electroceuticals, a division of springer nature America, Inc., SA special edition 2019 *Sci. Am.* **28** 76
[5] Rivnay J, Owens R M and Malliaras G G 2014 The rise of organic bioelectronics *Chem. Mater.* **26** 679–85
[6] Amdursky N, Głowacki E D and Meredith P 2019 Macroscale biomolecular electronics and ionics *Adv. Mater.* **31** 1802221
[7] Alvarez-Risco A, Del-Aguila-Arcentales S and Rosen M A 2022 Waste management and the circular economy, towards a circular economy *CSR, Sustainability, Ethics & Governance* ed A Alvarez-Risco, M A Rosen and S Del-Aguila-Arcentales (Springer) pp 119–21
[8] Ogunseitan O A, Schoenung J M, Lincoln J, Nguyen B H, Strauss K, Frost K, Schwartz E, He H and Ibrahim M 2022 Biobased materials for sustainable printed circuit boards *Nat. Rev. Mater.* **7** 749–50
[9] D'Ischia M *et al* 2013 Melanins and melanogenesis: methods, standards, protocols *Pigment Cell Melanoma Res.* **26** 616–33
[10] Pralea I E *et al* 2019 From extraction to advanced analytical methods: the challenges of melanin analysis *Int. J. Mol. Sci.* **20** 3943
[11] D'Ischia M, Napolitano A, Pezzella A, Meredith P and Sarna T 2009 Chemical and structural diversity in eumelanins: unexplored bio-optoelectronic materials *Angew. Chem., Int. Ed.* **48** 3914–21
[12] Mostert A B 2021 Melanin, the what, the why and the how: an introductory review for materials scientists interested in flexible and versatile polymers *Polymers* **13** 1670
[13] Abbas M, Ali M, Shah S K, D'Amico F, Postorino P, Mangialardo S, Guidi M C, Cricenti A and Gunnella R 2011 Control of structural, electronic, and optical properties of eumelanin films by electrospray deposition *J. Phys. Chem.* B **115** 11199–207
[14] Abbas M *et al* 2009 Structural, electrical, electronic and optical properties of melanin films *Eur. Phys. J.* E **28** 285–91
[15] Meredith P, Powell B J, Riesz J, Nighswander-Rempel S P, Pederson M R and Moore E G 2006 Towards structure-property-function relationships for eumelanin *Soft Matter* **2** 37–44
[16] Paulin J V, Coleone A P, Batagin-Neto A, Burwell G, Meredith P, Graeff C F O and Mostert A B 2021 Melanin thin-films: a perspective on optical and electrical properties *J. Mater. Chem.* C **9** 8345–58
[17] Solano F 2014 Melanins: skin pigments and much more—Types, structural models, biological functions, and formation routes *New J. Sci.* **2014** 1–28
[18] Xu R, Gouda A, Caso M F, Soavi F and Santato C 2019 Melanin: a greener route to enhance energy storage under solar light *ACS Omega* **4** 12244–51
[19] Felix C C, Hyde J S, Sarna T and Sealy R C 1978 Interactions of melanin with metal ions. Electron spin resonance evidence for chelate complexes of metal ions with free radicals *J. Am. Chem. Soc.* **100** 3922–6
[20] Al Khatib M, Costa J, Baratto M C, Basosi R and Pogni R 2020 Paramagnetism and relaxation dynamics in melanin biomaterials *J. Phys. Chem.* B **124** 2110–5
[21] Vasileiou T and Summerer L 2021 Vasileiou T and Summerer Erratum: a biomimetic approach to shielding from ionizing radiation: the case of melanized fungi *PLoS One* **16** e0257068
[22] Mostert A B 2022 The importance of water content on the conductivity of biomaterials and bioelectronic devices *J. Mater. Chem.* B **10** 7108–21
[23] Sheliakina M, Mostert A B and Meredith P 2018 Decoupling ionic and electronic currents in melanin *Adv. Funct. Mater.* **28** 1805514
[24] Ambrico M, Cardone A, Ligonzo T, Augelli V, Ambrico P F, Cicco S, Farinola G M, Filannino M, Perna G and Capozzi V 2010 Hysteresis-type current-voltage characteristics in Au/eumelanin/ITO/glass structure: towards melanin based memory devices *Org. Electron.* **11** 1809–14
[25] Ambrico M, Ambrico P F, Ligonzo T, Cardone A, Cicco S R, Lavizzera A, Augelli V and Farinola G M 2012 Memory-like behavior as a feature of electrical signal transmission in melanin-like bio-polymers *Appl. Phys. Lett.* **100** 253702
[26] Tehrani Z, Whelan S P, Mostert A B, Paulin J V, Ali M M, Ahmadi E D, Graeff C F O, Guy O J and Gethin D T 2020 Printable and flexible graphene pH sensors utilising thin film melanin for physiological applications *2D Mater.* **7** 024008
[27] Yang L, Guo X, Jin Z, Guo W, Duan G, Liu X and Li Y 2021 Emergence of melanin-inspired supercapacitors *Nano Today* **37** 101075
[28] Ambrico M, Ambrico P F, Cardone A, Ligonzo T, Cicco S R, Mundo R D, Augelli V and Farinola G M 2011 Melanin layer on silicon: an attractive structure for a possible exploitation in bio-polymer based metal-insulator-silicon devices *Adv. Mater.* **23** 3332–6
[29] Ambrico M *et al* 2013 Engineering polydopamine films with tailored behaviour for next-generation eumelanin-related hybrid devices *J. Mater. Chem.* C **1** 1018–28
[30] Xiao M, Shawkey M D and Dhinojwala A 2020 Bioinspired melanin-based optically active materials *Adv. Opt. Mater.* **8** 2000932
[31] Dong J, Sun J, Cai W, Guo C, Wang Q, Zhao X and Zhang R 2022 A natural cuttlefish melanin nanoprobe for

preoperative and intraoperative mapping of lymph nodes *Nanomedicine* **41** 102510
[32] Di Mauro E, Xu R, Soliveri G, Santato C, Physics E and Montréal P 2022 Natural melanin pigments and their interfaces with metal ions and oxides: emerging concepts and technologies *MRS Commun.* **7** 141–51
[33] Phua J W and Ottenheim C J H 2021 A method for obtaining melanin from invertebrate biomass and the product obtained therefrom *US20230127563A1*
[34] Surendra K C, Tomberlin J K, van Huis A, Cammack J A, Heckmann L H L and Khanal S K 2020 Rethinking organic wastes bioconversion: evaluating the potential of the black soldier fly (Hermetia illucens (L.)) (Diptera: stratiomyidae) (BSF) *Waste Manage.* **117** 58–80
[35] Wang Y S and Shelomi M 2017 Review of black soldier fly (Hermetia illucens) as animal feed and human food *Foods* **6** 91
[36] Martinez-Gonzalez J A, Cavaye H, McGettrick J D, Meredith P, Motovilov K A and Mostert A B 2021 Interfacial water morphology in hydrated melanin *Soft Matter* **17** 7940–52
[37] Nguyen K V *et al* 2023 The effect of direct electron beam patterning on the water uptake and ionic conductivity of nafion thin films *Adv. Electron. Mater.* **9** 2300199
[38] Abramov P A, Zhukov S S, Savinov M, Mostert A B and Motovilov K A 2023 The influence of copper ions on the transport and relaxation properties of hydrated eumelanin *Phys. Chem. Chem. Phys.* **25** 11601–12
[39] Herrig S, Thol M, Harvey A H and Lemmon E W 2018 A reference equation of state for heavy water *J. Phys. Chem. Ref. Data* **47** 043102
[40] Barsoukov E and Ross Macdonald J 2005 *Impedance Spectroscopy: Theory, Experiment, and Applications 2nd* ed E Barsoukov and J R Macdonald (Wiley)
[41] Bondarenko A S, Ragoisha G A and Pomerantsev A L 2005 *Progress in Chemometrics Research* (Nova Science Publishers) pp 89–102
[42] Eker B, Meissner R, Bertsch A, Mehta K and Renaud P 2013 Label-free recognition of drug resistance via impedimetric screening of breast cancer cells *PLoS One* **8** 1–12
[43] Randles E B and J B 1938 Kinetics of rapid electrode reactions *J. Chim. Phys.* **169** 157–65
[44] Bisquert J 2002 Theory of the impedance of electron diffusion and recombination in a thin layer *J. Phys. Chem.* B **106** 325–33
[45] Nguyen T Q and Breitkopf C 2018 Determination of diffusion coefficients using impedance spectroscopy data *J. Electrochem. Soc.* **165** E826–31
[46] Huang J 2018 Diffusion impedance of electroactive materials, electrolytic solutions and porous electrodes: warburg impedance and beyond *Electrochim. Acta* **281** 170–88
[47] Lasia A 2002 *Electrochemical Impedance Spectroscopy and Its Applications, Modern Aspects of Electrochemistry* (Kluwer Academic Publishers) pp 143–248
[48] Smith Sorensen T and Compan V 1995 Complex permittivity of a conducting, dielectric layer containing arbitrary binary nernst-planck electrolytes with applications to polymer films and cellulose acetate membranes *J. Chem. Soc. Faraday Trans.* **91** 4235–50
[49] Pal P and Ghosh A 2020 Broadband dielectric spectroscopy of BMPTFSI ionic liquid doped solid-state polymer electrolytes: coupled ion transport and dielectric relaxation mechanism *J. Appl. Phys.* **128** 084104
[50] Barjola A, Escorihuela J, García-Bernabé A, Sahuquillo Ó, Giménez E and Compañ V 2021 Diffusivity and free anion concentration of ionic liquid composite polybenzimidazole membranes *RSC Adv.* **11** 26379–90
[51] Funke K 1993 Jump relaxation in solid electrolytes *Prog. Solid State Chem.* **22** 111–95
[52] Natesan B, Karan N K and Katiyar R S 2006 Ion relaxation dynamics and nearly constant loss behavior in polymer electrolyte *Phys. Rev.* E **74** 042801
[53] Cole K S and Cole R H 1941 Dispersiona and absorption in dielectrics: I. Alternating current characteristics *J. Chem. Phys.* **9** 98–105
[54] Cole H S and Davidson D W 1951 Dielectric relaxation in glycerol, propylene glycol, and n-propanol *J. Chem. Phys.* **19** 1484
[55] Cole K S and Cole R H 1942 Dispersion and absorption in dielectrics: II. Direct current characteristics *J. Chem. Phys.* **10** 98–105
[56] Cole R H 1955 On the analysis of dielectric relaxation measurements *J. Chem. Phys.* **23** 493–9
[57] Havriliak S and Negami S 1966 A complex plane analysis of α-dispersions in some polymer systems *J. Polym. Sci.* **14** 99–117
[58] Ordinario D D, Phan L, Walkup IV W G, Jocson J M, Karshalev E, Hüsken N and Gorodetsky A A 2014 Bulk protonic conductivity in a cephalopod structural protein *Nat. Chem.* **6** 596–602
[59] Sidebottom D L 2009 Colloquium: understanding ion motion in disordered solids from impedance spectroscopy scaling *Rev. Mod. Phys.* **81** 999–1014
[60] Bard A J and Faulkner L R 2002 Electrochemical methods fundamentals and applications *Russ. J. Electrochem.* **38** 1364
[61] Dam T, Tripathy S N, Paluch M, Jena S S and Pradhan D K 2016 Investigations of relaxation dynamics and observation of nearly constant loss phenomena in PEO_{20}-$LiCF_3SO_3$-ZrO_2 based polymer nano-composite electrolyte *Electrochim. Acta* **202** 147–56
[62] Klein R J, Zhang S, Dou S, Jones B H, Colby R H and Runt J 2006 Modeling electrode polarization in dielectric spectroscopy: ion mobility and mobile ion concentration of single-ion polymer electrolytes *J. Chem. Phys.* **124** 144903
[63] Motovilov K A, Grinenko V, Savinov M, Gagkaeva Z V, Kadyrov L S, Pronin A A, Bedran Z V, Zhukova E S, Mostert A B and Gorshunov B P 2019 Redox chemistry in the pigment eumelanin as a function of temperature using broadband dielectric spectroscopy *RSC Adv.* **9** 3857–67
[64] Rienecker S B, Mostert A B, Schenk G, Hanson G R and Meredith P 2015 Heavy water as a probe of the free radical nature and electrical conductivity of melanin *J. Phys. Chem.* B **119** 14994–5000
[65] Das A, Thakur A K and Kumar K 2015 Origin of near constant loss (NCL) in ion conducting polymer blends *J. Phys. Chem. Solids* **80** 62–66
[66] Zhang Q, Liu X, Yin L, Chen P, Wang Y and Yan T 2018 Electrochemical impedance spectroscopy on the capacitance of ionic liquid–acetonitrile electrolytes *Electrochim. Acta* **270** 352–62
[67] Izgorodina E I, Forsyth M and MacFarlane D R 2009 On the components of the dielectric constants of ionic liquids: ionic polarization? *Phys. Chem. Chem. Phys.* **11** 2452–8
[68] Nakamura K, Saiwaki T and Fukao K 2010 Dielectric relaxation behavior of polymerized ionic liquid *Macromolecules* **43** 6092–8
[69] Matos B R, Politano R, Rey J F Q, Hermida-Merino D, Schade U, Puskar L and Fonseca F C 2018 Interplay of α/β-Relaxation dynamics and the shape of ionomer building blocks *Sci. Rep.* **8** 13441
[70] Tierney N K and Register R A 2002 Ion hopping in ethylene-methacrylic acid ionomer melts as probed by rheometry and cation diffusion measurements *Macromolecules* **35** 2358–64
[71] Matos B R, Santiago E I, Rey J F Q, Scuracchio C H, Mantovani G L, Hirano L A and Fonseca F C 2015 Dc Proton conductivity at low-frequency in Nafion conductivity

spectrum probed by time-resolved SAXS measurements and impedance spectroscopy *J. Polym. Sci.* B **53** 822–8
[72] Colby R H, Zheng X, Rafailovich M H, Sokolov J, Peiffer D G, Schwarz S A, Strzhemechny Y and Nguyen D 1998 Dynamics of lightly sulfonated polystyrene ionomers *Phys. Rev. Lett.* **81** 3876–9
[73] Matos B R, da Silva J S, Santiago E I, Parra D F, Carastan D J, de Florio D Z, Andrada H E, Carreras A C and Fonseca F C 2017 Proton and cesium conductivity in perfluorosulfonate ionomers at low and high relative humidity *Solid State Ion.* **301** 86–94
[74] Mostert A B, Rienecker S B, Sheliakina M, Zierep P, Hanson G R, Harmer J R, Schenk G and Meredith P 2020 Engineering proton conductivity in melanin using metal doping *J. Mater. Chem.* B **8** 8050–60
[75] Bedran Z V, Zhukov S S, Abramov P A, Tyurenkov I O, Gorshunov B P, Mostert B and Motovilov K A 2021 Water-activated semiquinone formation and carboxylic acid dissociation in melanin revealed by infrared spectroscopy *Polymers* **13** 4403
[76] Mostert A B, Powell B J, Pratt F L, Hanson G R, Sarna T, Gentle I R, Meredith P and Hoffman B M 2012 Role of semiconductivity and ion transport in the electrical conduction of melanin *Proc. Natl Acad. Sci. USA* **109** 209
[77] Wang Y, Sun C N, Fan F, Sangoro J R, Berman M B, Greenbaum S G, Zawodzinski T A and Sokolov A P 2013 Examination of methods to determine free-ion diffusivity and number density from analysis of electrode polarization *Phys. Rev.* E **87** 042308
[78] D'Amora U *et al* 2022 Eumelanin from the black soldier fly as sustainable biomaterial: characterisation and functional benefits in tissue-engineered composite scaffolds *Biomedicines* **10** 2945